The Aeronautical Journal (2026), **130**, pp. 2319–2342
doi:10.1017/aer.2026.10162

RESEARCH ARTICLE

Transonic buffeting control via a nonlinear aeroservoelastic model of reduced-order

Zhijun Yang[1], Zhong Zhang[1], Mingming Zhang[2] and Shun He[2]

[1]Beijing Institute of Structure and Environment Engineering, Beijing, China
[2]Northwestern Polytechnical University, Xian, China
Corresponding author: Zhijun Yang; Email: yangzhijun@nuaa.edu.cn

Received: 1 July 2025; **Revised:** 10 March 2026; **Accepted:** 10 March 2026

Keywords: aeroservoelastic buffeting; buffeting control; nonlinear reduced-order model; nonlinear system identification

Abstract

The paper presents a detailed study on the transonic buffeting phenomenon and related active control problems via a novel nonlinear aeroservoelastic model of reduced-order. An important feature of the study is the reconstruction of the unsteady aerodynamics in transonic buffeting flows via a modified nonlinear state-space identification scheme. Based on the aerodynamic model reduction, the paper gives a nonlinear aeroservoelastic model of reduced-order by coupling the structural dynamics of a wing section with a control surface. To demonstrate the accuracy and efficiency of the above model and the control design for transonic buffeting, the study deals with detailed numerical simulations of a wing section of an NACA0012 aerofoil system with a control surface. The case studies cover the dynamic behaviours of such an aerofoil system, including flutter, limit-cycle oscillations, nodal-shaped oscillations and open/closed-loop aeroservoelastic buffeting oscillations. The numerical results demonstrate that the novel nonlinear reduced-order modeling approach provides an efficient way to synthesise the active buffeting control system. Based on the nonlinear aeroservoelastic model of reduced-order, the control gains of the buffeting controller can be efficiently determined and the unstable buffeting behaviours can also be controlled effectively.

Nomenclature

$\boldsymbol{A}_a, \boldsymbol{B}_a, \boldsymbol{C}_a, \boldsymbol{D}_a, \boldsymbol{E}_a, \boldsymbol{F}_a, \boldsymbol{G}_a, \boldsymbol{H}_a$	coefficients matrices of the reduced-order model
$\boldsymbol{x}_a, \boldsymbol{u}, \boldsymbol{y}_a$	state vector, input vector, and output vector
sinh	hyperbolicsine function
$\boldsymbol{x}_0, \boldsymbol{u}_0$	scale factors
$\|\boldsymbol{e}\|_2$	Euclidean norm of the output error
$\bar{x}_\alpha, \bar{r}_\alpha$	structural parameters
V_∞^*, V_∞	reduced velocity, free-stream velocity
$\bar{S}_{s\beta}$	dimensionless inertial coupling
b	half-chord length
$k_\beta, \zeta_\beta, \omega_\beta, \beta_c$	actuation parameters
y_s	acceleration signal
$\boldsymbol{A}_s^d, \boldsymbol{B}_c^d, \boldsymbol{B}_q^d$	matrices of the discrete dynamic model
a_i, b_i	unknown coefficients of ASE system
w	output noise
$\bar{b}_0$	estimated value
$\boldsymbol{L}$	observer gain
$\boldsymbol{K}_r$	controller gain
T_s	sampling time
k	time step

© The Author(s), 2026. Published by Cambridge University Press on behalf of Royal Aeronautical Society.

https://doi.org/10.1017/aer.2026.10162 Published online by Cambridge University Press

Greek symbol

α	angle-of-attack
β	angle of control surface
$\boldsymbol{\Phi}$	nonlinear mapping
λ	regularisation parameter
ω_h, ω_α	natural frequencies
μ	mass ratio
ζ_β	damping ratio
f	sum of the unknown disturbances
ω_o, ω_c	bandwidth of the linear ESO and controller

1.0 Introduction

Active aeroelastic control has been recognised as an integrated methodology derived from advancements in aeroelastic mechanics and control theory, serving to suppress structural instabilities while optimising aircraft weight parameters. Over recent decades, substantial research efforts have been devoted to developing active flutter suppression systems and limit-cycle oscillation (LCO) control architectures [1–6], with experimental verifications successfully conducted in wind tunnel facilities [7–9]. Nevertheless, the application of active control paradigms to transonic buffet-induced structural vibrations remains insufficiently addressed.

Buffet phenomena – characterised by self-sustained shock oscillations in static aerofoils under specific Mach numbers, aerodynamic profiles and angles of attack [10, 11] – are fundamentally attributed to unsteady flow separation and dynamic shock interactions. The resultant structural vibrations, termed buffeting [12, 13], have motivated research into flow manipulation strategies for buffet mitigation [14, 15]. Current methodologies predominantly focus on aerodynamic instability suppression through devices such as vortex generators (VGs), with structural coupling effects often treated as secondary considerations. In representative work by Caruana et al. [16], both upstream-positioned VGs and trailing-edge deflectors (TEDs) were demonstrated to reduce buffet intensity and structural oscillations, though VGs were found to compromise aerodynamic efficiency while TEDs exhibited implementation challenges in three-dimensional configurations. Gao et al. [17] implemented a linear-delayed control law utilising lift coefficient feedback, achieving buffet suppression through three adjustable parameters. However, structural instability mitigation was not addressed, and the computational fluid dynamics (CFD)-dependent framework limited practical implementation feasibility.

Due to the high costs of both wind tunnel tests and CFD, it is preferable to explore the numerical simulations of active aeroelastic control based on the reduced-order models (ROMs). One type of the ROMs is based on the manipulation of the governing equations, which consists of a systematic procedure to generate both linear and nonlinear ROMs [18–20], but the added complexity in the model implementation makes it hard to use. The more practical type of approaches is based on the system identifications in order to replace the high-fidelity model with a black box of lower dimensions. For the system identifications, these approaches of the aeroservoelastic (ASE) modeling of reduced-order can also be divided into linear approaches [21–24] and nonlinear approaches [25–27]. Ghoreyshi et al. gave a comparison of different nonlinear ROMs for computing the unsteady and nonlinear aerodynamic loads in the transonic region using the X-31 configuration as the verification model [28]. Their results showed that the four approaches, namely Duhamel's superposition integral using indicial (step) response functions, Volterra theory using nonlinear kernels, radial basis functions and a surrogate-based recurrence framework, could produce accurate results, and the nonlinear model based on indicial functions reached the best accuracy. Huang et al. presented a parallel cascade ROM established via the predictor-based subspace scheme [29] to investigate the open-/closed-loop ASE behaviours of the Benchmark Active Control Technology wing. However, the accuracy of the ROM in predicting the LCO behaviours needs to be improved further because of the overfitting problem for identifying the nonlinear neural network in the ROM. Recently, Huang et al. developed a two-stage training procedure for a novel transonic ASE

https://doi.org/10.1017/aer.2026.10162 Published online by Cambridge University Press

ROM with direct effects from the structural movements to the aerodynamic loads taken into account [30], but the numerical simulations focused on some basic aeroelastic and ASE phenomena, such as flutter, the LCOs and the frequency responses. Hence, the current studies on ROMs have not dealt well with the aerodynamic instabilities, including the structural vibration control with buffeting based on ROMs.

The purpose of this study is to explore the transonic buffeting control based on a nonlinear aeroelastic model of reduced-order with high efficiency and high precision compared with CFD. The rest of the paper is organised as follows. The modified nonlinear ROM is established in Section 2.0 for an ASE system of three degrees of freedom. Then, the active buffeting controller is presented in Section 3.0. To demonstrate the accuracy of the ASE ROM in predicting aeroelastic and ASE phenomena, detailed comparisons are made in Section 4.0 for LCOs, nodal-shaped oscillations, frequency responses and ASE vibrations in a buffet flow as illustrative examples. The performance of the controller is also verified in this section. Finally, a few concluding remarks are drawn in Section 5.0.

2.0 Nonlinear aeroservoelastic modeling of reduced-order

This section aims to construct a nonlinear ASE ROM for the transonic ASE systems. The presented approach features a modified state-space-based ROM suitable for describing the ASE systems subject to both structural vibrations and control surface motions. The section begins with the introduction of a modified nonlinear ROM and ends with the establishment of the nonlinear ASE ROM.

2.1 Reduced-order aerodynamic modeling in transonic buffeting flows

This subsection presents a state-space-based ROM to capture the linear and nonlinear characteristics of transonic unsteady aerodynamic forces accurately. The structure of the modified nonlinear ROM is defined as the following state equations in a vector form

$$\begin{aligned} \boldsymbol{x}_a(k+1) &= \boldsymbol{A}_a\boldsymbol{x}_a(k) + \boldsymbol{B}_a\boldsymbol{u}(k) + \boldsymbol{E}_a\boldsymbol{\Phi}\left(\mathrm{diag}\left(\boldsymbol{x}_0\right)\boldsymbol{x}_a(k)\right) + \boldsymbol{F}_a\boldsymbol{\Phi}\left(\mathrm{diag}\left(\boldsymbol{u}_0\right)\boldsymbol{u}(k)\right) \\ \boldsymbol{y}_a(k) &= \boldsymbol{C}_a\boldsymbol{x}_a(k) + \boldsymbol{D}_a\boldsymbol{u}(k) + \boldsymbol{G}_a\boldsymbol{\Phi}\left(\mathrm{diag}\left(\boldsymbol{x}_0\right)\boldsymbol{x}_a(k)\right) + \boldsymbol{H}_a\boldsymbol{\Phi}\left(\mathrm{diag}\left(\boldsymbol{u}_0\right)\boldsymbol{u}(k)\right) \end{aligned} \tag{1}$$

where $\boldsymbol{x}_a \in \mathbb{R}^n$, $\boldsymbol{u} \in \mathbb{R}^p$ and $\boldsymbol{y}_a \in \mathbb{R}^q$ are the state vector, the input vector, and the output vector, respectively. In this paper, the displacements are used as the input vector $\boldsymbol{u}$ and the aerodynamic forces are used as the output vector $\boldsymbol{y}_a$. The influences of various time derivatives of the displacements on the aerodynamic forces are implicitly captured within the state-space model. Therefore, these derivative terms do not need to be explicitly included in the inputs. The coefficient matrices $(\boldsymbol{A}_a, \boldsymbol{B}_a, \boldsymbol{C}_a, \boldsymbol{D}_a)$ of the linear part in Equation (1) are constants to be identified via the eigensystem realisation algorithm (ERA), and the coefficients matrices $(\boldsymbol{E}_a,\ \boldsymbol{F}_a,\ \boldsymbol{G}_a,\ \boldsymbol{H}_a)$ of the nonlinear part are constants to be determined via the Levenberg-Marquardt (LM) algorithm [31]. Here, $\boldsymbol{\Phi}(\cdot)$ is the vector of nonlinear mapping with the entries assumed as a hyperbolicsine function $\sinh(\cdot)$ so as to accurately model the complex transonic aerodynamic forces due to different amplitudes of structural vibrations and buffeting flows. As the hyperbolicsine function $\sinh(\cdot)$ is a strictly increasing function, the scale factors $\boldsymbol{x}_0$ and $\boldsymbol{u}_0$ are identified in the optimisation produce for the state vector and the input vector to properly describe nonlinearities.

According to the structure of Equation (1), the identification process of the above nonlinear ROM can be constructed as shown in Fig. 1, where the parameters of the linear model are respectively identified and selected via the impulsive signal and the sinusoidal signal generated via CFD codes first, and then are kept as constants while the parameters of the nonlinear part are determined via the filtered white Gaussian noise (FWGN) signal produced via CFD.

To construct the nonlinear ROM in Equation (1), the first stage is to identify the coefficient matrices $\boldsymbol{A}_a$, $\boldsymbol{B}_a$, $\boldsymbol{C}_a$ and $\boldsymbol{D}_a$ in the linear ROM via ERA. For this purpose, the discrete-time impulsive and sinusoidal response signals generated via CFD are used as the training and validation signals, respectively. The detailed identification procedure can be found in Ref. [32].

https://doi.org/10.1017/aer.2026.10162 Published online by Cambridge University Press

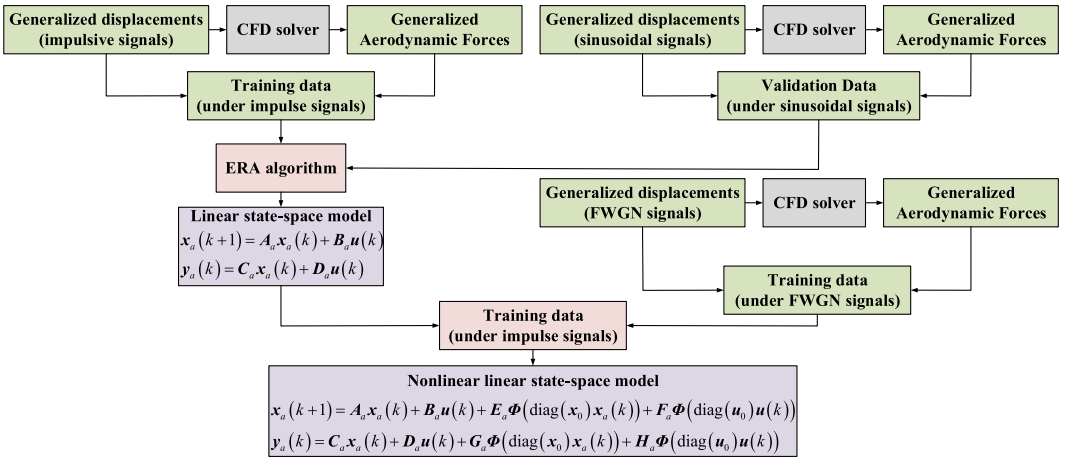


Figure 1. *Flow chart of identification of a nonlinear ROM.*

After the above matrices of the linear part are estimated, the next step is to keep the matrices unchanged and use the LM algorithm to determine the optimised parameters in the nonlinear part. The entries in matrices $\boldsymbol{x}_0$, $\boldsymbol{u}_0$, $\boldsymbol{E}_a$, $\boldsymbol{F}_a$, $\boldsymbol{G}_a$ and $\boldsymbol{H}_a$ can be collected as an unknown vector $\boldsymbol{p}$ of dimension $(n+p)\times(n+q)+p+q$. Subsequently, the following ordinary differential equations corresponding to vector $\boldsymbol{p}$ should be solved until the output error $\boldsymbol{e}_k=\boldsymbol{y}_{\mathrm{CFD}}(k)-\boldsymbol{y}_a(k;\boldsymbol{p})$ is small enough. That is, vector $\boldsymbol{p}$ yields

$$\begin{aligned}
\boldsymbol{x}_a^{k+1}&=\boldsymbol{A}_a\boldsymbol{x}_a^k+\boldsymbol{B}_a\boldsymbol{u}^k+\boldsymbol{E}_a\boldsymbol{\Phi}\left(\boldsymbol{x}_0,\boldsymbol{x}_a^k\right)+\boldsymbol{F}_a\boldsymbol{\Phi}\left(\boldsymbol{u}_0,\boldsymbol{u}^k\right)\\
\boldsymbol{x}_{a/\boldsymbol{p}}^{k+1}&=\boldsymbol{A}_a\boldsymbol{x}_{a/\boldsymbol{p}}^k+\boldsymbol{E}_{a/\boldsymbol{p}}\boldsymbol{\Phi}\left(\boldsymbol{x}_0,\boldsymbol{x}_a^k\right)+\boldsymbol{E}_a\boldsymbol{\Phi}\left(\boldsymbol{x}_0,\boldsymbol{x}_a^k\right)_{/\boldsymbol{p}}+\boldsymbol{F}_{a/\boldsymbol{p}}\boldsymbol{\Phi}\left(\boldsymbol{u}_0,\boldsymbol{u}^k\right)+\boldsymbol{F}_a\boldsymbol{\Phi}\left(\boldsymbol{u}_0,\boldsymbol{u}^k\right)_{/\boldsymbol{p}}\\
\boldsymbol{y}_a^k&=\boldsymbol{C}_a\boldsymbol{x}_a^k+\boldsymbol{D}_a\boldsymbol{u}^k+\boldsymbol{G}_a\boldsymbol{\Phi}\left(\boldsymbol{x}_0,\boldsymbol{x}_a^k\right)+\boldsymbol{H}_a\boldsymbol{\Phi}\left(\boldsymbol{u}_0,\boldsymbol{u}^k\right)\\
\boldsymbol{y}_{a/\boldsymbol{p}}^k&=\boldsymbol{C}_a\boldsymbol{x}_{a/\boldsymbol{p}}^k+\boldsymbol{G}_{a/\boldsymbol{p}}\boldsymbol{\Phi}\left(\boldsymbol{x}_0,\boldsymbol{x}_a^k\right)+\boldsymbol{G}_a\boldsymbol{\Phi}\left(\boldsymbol{x}_0,\boldsymbol{x}_a^k\right)_{/\boldsymbol{p}}+\boldsymbol{H}_{a/\boldsymbol{p}}\boldsymbol{\Phi}\left(\boldsymbol{u}_0,\boldsymbol{u}^k\right)+\boldsymbol{H}_a\boldsymbol{\Phi}\left(\boldsymbol{u}_0,\boldsymbol{u}^k\right)_{/\boldsymbol{p}}
\end{aligned}\tag{2}$$

where

$$\begin{aligned}
&\boldsymbol{\chi}_{/\boldsymbol{p}}=\frac{\partial\boldsymbol{\chi}}{\partial\boldsymbol{p}},\quad \boldsymbol{\chi}=\boldsymbol{x}_a,\boldsymbol{y}_a,\boldsymbol{E}_a,\boldsymbol{F}_a,\boldsymbol{G}_a,\boldsymbol{H}_a,\boldsymbol{\Phi}\\
&\boldsymbol{\Phi}(\boldsymbol{\delta}_0,\boldsymbol{\delta})_{/\boldsymbol{p}}=\frac{\partial\boldsymbol{\Phi}\left(\boldsymbol{\delta}_0,\boldsymbol{\delta}\right)}{\partial\boldsymbol{\delta}_0}\frac{\partial\boldsymbol{\delta}_0}{\partial\boldsymbol{p}}+\frac{\partial\boldsymbol{\Phi}\left(\boldsymbol{\delta}_0,\boldsymbol{\delta}\right)}{\partial\boldsymbol{\delta}}\frac{\partial\boldsymbol{\delta}}{\partial\boldsymbol{p}},\boldsymbol{\delta}=\boldsymbol{x},\boldsymbol{u}
\end{aligned}\tag{3}$$

The unknown vector $\boldsymbol{p}$ is updated at each iteration via the following least-square problem [33]

$$\left(\boldsymbol{J}^{\mathrm{T}}\boldsymbol{J}+\lambda\boldsymbol{I}\right)\Delta\boldsymbol{p}=-\boldsymbol{J}^{\mathrm{T}}\boldsymbol{e}\tag{4}$$

where λ is a regularisation parameter used to keep the left-hand-side matrix always nonsingular. The expansions of vectors in Equation (4) are evaluated as

$$\boldsymbol{e}=\begin{Bmatrix}\boldsymbol{e}_1\\ \boldsymbol{e}_2\\ \vdots\\ \boldsymbol{e}_m\end{Bmatrix},\quad \boldsymbol{J}=\begin{bmatrix}\boldsymbol{e}_{1/\boldsymbol{p}}\\ \boldsymbol{e}_{2/\boldsymbol{p}}\\ \vdots\\ \boldsymbol{e}_{m/\boldsymbol{p}}\end{bmatrix}=-\begin{bmatrix}\boldsymbol{y}_{a/\boldsymbol{p}}(1)\\ \boldsymbol{y}_{a/\boldsymbol{p}}(2)\\ \vdots\\ \boldsymbol{y}_{a/\boldsymbol{p}}(m)\end{bmatrix}\tag{5}$$

The iteration stops when either the Euclidean norm of the output error $\|\boldsymbol{e}\|_2$ achieves a sufficiently small value or the variation between two iterations is smaller than a user-defined threshold.

https://doi.org/10.1017/aer.2026.10162 Published online by Cambridge University Press

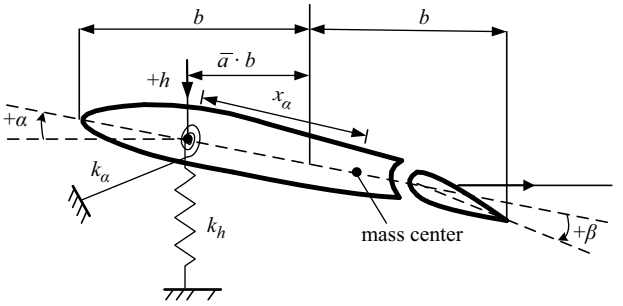


Figure 2. *Aerofoil system with a control surface.*

2.2 Nonlinear aeroservoelastic modeling

This subsection deals with the dynamic modeling for a two-dimensional aerofoil system having a control surface shown in Fig. 2. The aerofoil system has three degrees of freedom, that is, the plunge, the pitch and the control surface motion, and the mean angle-of-attack is zero. The three-degree-of-freedom dynamic equations of NACA0012 aerofoil were established in Ref. [34] and subsequently simplified in Ref. [35] based on the assumption of sufficiently large stiffness for the control surface degree of freedom. The dynamic equations in this paper are also derived from this assumption, and the motion of the control surface is assumed to be unaffected by aerodynamic forces and inertial coupling with other degrees of freedom. With the help of the Lagrange equation of the second kind and the dimensionless structural time $\tau = \omega_\alpha t$, it is easy to establish the dynamic equation of the aerofoil as follows

$$\boldsymbol{M}\ddot{\boldsymbol{\xi}} + \boldsymbol{K}\boldsymbol{\xi} = \boldsymbol{S}\ddot{\beta} + \boldsymbol{f} \tag{6}$$

The vectors and matrices in Equation (6) read

$$\boldsymbol{M} = \begin{bmatrix} 1 & \bar{x}_\alpha \\ \bar{x}_\alpha & \bar{r}_\alpha^2 \end{bmatrix}, \quad \boldsymbol{K} = \begin{bmatrix} (\omega_h/\omega_\alpha)^2 & 0 \\ 0 & \bar{r}_\alpha^2 \end{bmatrix}, \quad \boldsymbol{\xi} = \begin{Bmatrix} \xi_1 \\ \xi_2 \end{Bmatrix} = \begin{Bmatrix} h/b \\ \alpha \end{Bmatrix}, \; \boldsymbol{S} = -\begin{Bmatrix} \bar{S}_{h\beta} \\ \bar{S}_{\alpha\beta} \end{Bmatrix},$$

$$\boldsymbol{f} = \frac{\left(V_\infty^*\right)^2}{\pi} \begin{Bmatrix} -C_l \\ 2C_m \end{Bmatrix} \tag{7}$$

where $\bar{x}_\alpha$ represents the static unbalance of the aerofoil, which is the dimensionless distance between the mass centre and the stiffness centre, $\bar{r}_\alpha$ is the gyration radius of the aerofoil around the elastic axis ω_h and ω_α are the natural frequencies of the plunge and pitch, respectively. b is the half-chord length, and $V_\infty^* = V_\infty / \left(\omega_\alpha b \sqrt{\mu}\right)$ represents the reduced velocity. V_∞ denotes the free-stream velocity, and $\mu = m/\pi \rho_\infty b^2$ denotes the mass ratio. $\bar{S}_{h\beta}$ is the dimensionless inertial coupling between the plunge and the control surface motion, and $\bar{S}_{\alpha\beta}$ is the dimensionless inertial coupling between the pitch and the control surface motion. The lift coefficient C_l and the moment coefficient C_m are the entries in the output vector $\boldsymbol{y}_a$ in Section 2.1. Therefore, the inputs to the reduced-order aerodynamic model are plunge, pitch and control surface motion, while the outputs are lift coefficient and moment coefficient.

In general, the deflection angle of the control surface cannot respond to a control input instantaneously. Therefore, the dynamic model of the control surface under actuation is expressed as

$$\ddot{\beta} + 2\omega_\beta \zeta_\beta \dot{\beta} + \omega_\beta^2 \beta = k_\beta \omega_\beta^2 \beta_c \tag{8}$$

where k_β, ζ_β, ω_β, and β_c are the input gain, the damping ratio, the natural frequency and the control command, respectively. By combining Equations (6), (7) and (8), the dynamic model of the two-dimensional aerofoil system with a control surface is formulated as

$$\dot{\boldsymbol{x}}_s = \boldsymbol{A}_s \boldsymbol{x}_s + \boldsymbol{B}_c \beta_c + \boldsymbol{B}_q \boldsymbol{f} \tag{9}$$

https://doi.org/10.1017/aer.2026.10162 Published online by Cambridge University Press

where the vectors and matrices are defined as

$$\boldsymbol{A}_s = \begin{bmatrix} \mathbf{0}_{3\times3} & \boldsymbol{I}_3 \\ -\boldsymbol{M}_s{}^{-1}\boldsymbol{K}_s & -\boldsymbol{M}_s{}^{-1}\boldsymbol{C}_s \end{bmatrix}, \quad \boldsymbol{B}_c = \begin{bmatrix} \mathbf{0}_{3\times1} \\ -\boldsymbol{M}_s{}^{-1}\tilde{\boldsymbol{B}} \end{bmatrix}, \quad \boldsymbol{B}_q = \begin{bmatrix} \mathbf{0}_{3\times2} \\ \boldsymbol{M}_s{}^{-1}\left[\boldsymbol{I}_2; \mathbf{0}_{1\times2}\right] \end{bmatrix},$$

$$\boldsymbol{x}_s = \begin{bmatrix} \xi_1 & \xi_2 & \beta & \dot{\xi}_1 & \dot{\xi}_2 & \dot{\beta} \end{bmatrix}^T \tag{10}$$

The definitions of matrices $\boldsymbol{M}_s$, $\boldsymbol{C}_s$, $\boldsymbol{K}_s$ and $\tilde{\boldsymbol{B}}$ are, respectively, given as

$$\begin{gathered} \boldsymbol{M}_s = \begin{bmatrix} 1 & \bar{x}_\alpha & 0 \\ \bar{x}_\alpha & \bar{r}_\alpha^2 & 0 \\ 0 & 0 & 1 \end{bmatrix}, \ \boldsymbol{C}_s = \begin{bmatrix} 0 & 0 & -2\omega_\beta\zeta_\beta\bar{S}_{h\beta} \\ 0 & 0 & -2\omega_\beta\zeta_\beta\bar{S}_{\alpha\beta} \\ 0 & 0 & 2\zeta_\beta\omega_\beta \end{bmatrix}, \\ \boldsymbol{K}_s = \begin{bmatrix} (\omega_h/\omega_\alpha)^2 & 0 & -\omega_\beta^2\bar{S}_{h\beta} \\ 0 & \bar{r}_\alpha^2 & -\omega_\beta^2\bar{S}_{\alpha\beta} \\ 0 & 0 & \omega_\beta^2 \end{bmatrix}, \ \tilde{B} = \begin{Bmatrix} k_\beta\omega_\beta^2\bar{S}_{h\beta} \\ k_\beta\omega_\beta^2\bar{S}_{h\beta} \\ k_\beta\omega_\beta^2 \end{Bmatrix} \end{gathered} \tag{11}$$

To design the control law and analyse the aerofoil system under control, the structure accelerations are used as the feedback signals. The output equation of the controlled aerofoil system reads

$$y_s = \begin{bmatrix} b & x_c \end{bmatrix} \begin{bmatrix} \mathbf{0}_{2\times3} & \boldsymbol{I}_2 & \mathbf{0}_{2\times1} \end{bmatrix} \dot{x}_s \tag{12}$$

where x_c is the distance between the accelerometer and the elastic axis, y_s is the acceleration signal used to analyse the controlled aerofoil system.

To establish the ASE model, the dynamic model needs to be rebuilt in the discrete-time step as follows

$$\begin{aligned} \boldsymbol{x}_s\,(k+1) &= \boldsymbol{A}_s^d\boldsymbol{x}_s(k) + \boldsymbol{B}_c^d\beta_c(k) + \boldsymbol{B}_q^d\boldsymbol{f}(k) \\ y_s(k) &= \begin{bmatrix} b & x_c \end{bmatrix} \begin{bmatrix} \mathbf{0}_{2\times3} & \boldsymbol{I}_2 & \mathbf{0}_{2\times1} \end{bmatrix} \dot{x}_s(k) \\ &= \begin{bmatrix} b & x_c \end{bmatrix} \begin{bmatrix} \mathbf{0}_{2\times3} & \boldsymbol{I}_2 & \mathbf{0}_{2\times1} \end{bmatrix} \left(\boldsymbol{A}_s\boldsymbol{x}_s(k) + \boldsymbol{B}_c\beta_c(k) + \boldsymbol{B}_q\boldsymbol{f}(k)\right) \end{aligned} \tag{13}$$

where $\boldsymbol{A}_s^d$, $\boldsymbol{B}_c^d$ and $\boldsymbol{B}_q^d$ are the matrices corresponding to the discrete dynamic model. The final discrete equations of the reduced-order ASE system can be formulated as

$$\begin{aligned} &\boldsymbol{x}_a\,(k+1) = \boldsymbol{A}_a\boldsymbol{x}_a(k) + \boldsymbol{B}_a\boldsymbol{u}(k) + \boldsymbol{E}_a\boldsymbol{\Phi}\,(\mathrm{diag}\,(\boldsymbol{x}_0)\,\boldsymbol{x}_a(k)) + \boldsymbol{F}_a\boldsymbol{\Phi}\,(\mathrm{diag}\,(\boldsymbol{u}_0)\,\boldsymbol{u}(k)) \\ &\boldsymbol{y}_a(k) = \boldsymbol{C}_a\boldsymbol{x}_a(k) + \boldsymbol{D}_a\boldsymbol{u}(k) + \boldsymbol{G}_a\boldsymbol{\Phi}\,(\mathrm{diag}\,(\boldsymbol{x}_0)\,\boldsymbol{x}_a(k)) + \boldsymbol{H}_a\boldsymbol{\Phi}\,(\mathrm{diag}\,(\boldsymbol{u}_0)\,\boldsymbol{u}(k)) \\ &\boldsymbol{x}_s\,(k+1) = \boldsymbol{A}_s^d\boldsymbol{x}_s(k) + \boldsymbol{B}_c^d\beta_c(k) + \boldsymbol{B}_q^d\boldsymbol{f}(k) \\ &y_s(k) = \begin{bmatrix} b & x_c \end{bmatrix} \begin{bmatrix} \mathbf{0}_{2\times3} & \boldsymbol{I}_2 & \mathbf{0}_{2\times1} \end{bmatrix} \left(\boldsymbol{A}_s\boldsymbol{x}_s(k) + \boldsymbol{B}_c\beta_c(k) + \boldsymbol{B}_q\boldsymbol{f}(k)\right) \\ &\boldsymbol{u}(k) = \begin{bmatrix} \mathbf{1}_{3\times1} & \mathbf{0}_{3\times1} \end{bmatrix} \boldsymbol{x}_s(k),\ \boldsymbol{f}(k) == \frac{\left(V_\infty^*\right)^2}{\pi}\boldsymbol{y}_a(k) \end{aligned} \tag{14}$$

To improve the accuracy of aeroelastic response prediction, the predictor/corrector scheme [36] can be used in Equation (14).

3.0 Control law design for transonic buffeting control

Because of the instability and strong nonlinearity of the transonic aerodynamic forces, it is difficult to synthesise an active buffeting controller to remove instabilities in a buffet flow over a wide range of reduced velocities. In this study, an error-based control law is presented to control the structural vibration of the aerofoil system at different reduced velocities. The control law is synthesised based on the theory

https://doi.org/10.1017/aer.2026.10162 Published online by Cambridge University Press

of active disturbance rejection control (ADRC), which was first proposed by Han [37] and linearised by Gao et al. [38]. The linear ADRC reduces the number of parameters to be adjusted and makes the control theory to be easily analysed and designed. The linear ADRC for transonic active flutter suppression can be found in the previous studies of the authors in Refs [39, 40], where the control performance has been well studied via numerical simulations.

3.1 Design of the linear extended state observer

It is well known that the linearised mathematical model of a single-input/single-output (SISO) ASE system can be expressed in the form of a transfer function as

$$\frac{y_s(s)}{\beta_c(s)} = \frac{b_r s^r + \cdots + b_{n+1}s^{n+1} + b_n s^n + b_{n-1}s^{n-1} + \cdots + b_1 s + b_0}{a_r s^r + \cdots + a_{n+1}s^{n+1} + s^n + a_{n-1}s^{n-1} + \cdots + a_1 s + a_0}, \quad r \geq n \tag{15}$$

where a_i and b_i, $i = 1, 2 \cdots r$ are the unknown coefficients. However, the ASE system is nonlinear due to the nonlinearity and instability of the aerodynamic forces. The nonlinear ASE system can be rewritten in the time domain as

$$y_s^{(n)} = f\left(y_s, \dot{y}_s, \cdots, y_s^{(n-1)}, y_s^{(n+1)} \cdots, y_s^{(r)}, \dot{\beta}_c, \cdots \beta_c^{(n)}, \beta_c^{(n+1)}, \cdots \beta_c^{(r)}, w, t\right) + b_0\beta_c \tag{16}$$

where w is the output noise and f is the sum of the unknown disturbances, including not only the external disturbances but also the internal structure uncertainties. If the exact value b_0 is not available, the estimated value $\bar{b}_0$ should be introduced to design the control system, and Equation (16) can be recast as

$$y_s^{(n)} = \bar{f} + \bar{b}_0\beta_c \tag{17}$$

where

$$\bar{f} = f\left(y_s, \dot{y}_s, \cdots, y_s^{(n-1)}, y_s^{(n+1)} \cdots, y_s^{(r)}, \dot{\beta}_c, \cdots \beta_c^{(n)}, \beta_c^{(n+1)}, \cdots \beta_c^{(r)}, w, t\right) + b_0\beta_c - \bar{b}_0\beta_c \tag{18}$$

By defining the following extended state vector

$$\boldsymbol{x} = \begin{bmatrix} y_s & \dot{y}_s & \cdots & y_s^{(n-1)}\bar{f} \end{bmatrix}^T \tag{19}$$

the state-space form of Equation (17) can be expressed as

$$\begin{aligned} \dot{x} &= \boldsymbol{A}\boldsymbol{x} + \boldsymbol{B}\beta_c + \boldsymbol{E}\dot{\bar{f}} \\ y_s &= \boldsymbol{C}\boldsymbol{x} \end{aligned} \tag{20}$$

where

$$\boldsymbol{A} = \begin{bmatrix} 0 & 1 & 0 & \cdots & 0 \\ 0 & 0 & 1 & \cdots & 0 \\ \vdots & \vdots & \vdots & \ddots & \vdots \\ 0 & 0 & 0 & \cdots & 1 \\ 0 & 0 & 0 & \cdots & 0 \end{bmatrix}, \boldsymbol{B} = \begin{bmatrix} 0 \\ 0 \\ \vdots \\ \bar{b}_0 \\ 0 \end{bmatrix}, \boldsymbol{E} = \begin{bmatrix} 0 \\ 0 \\ \vdots \\ 0 \\ 1 \end{bmatrix}, \boldsymbol{C} = \begin{bmatrix} 1 & 0 & 0 & \cdots & 0 \end{bmatrix} \tag{21}$$

The state vector $\boldsymbol{x}$ can be divided into two parts. The first part $\boldsymbol{x}_1 = \begin{bmatrix} y_s & \dot{y}_s & \cdots & y_s^{(n-1)} \end{bmatrix}^{\mathrm{T}}$ represents the output signal and its time derivative. The second part $\boldsymbol{x}_2 = [x_{n+1}] = \left[\bar{f}\right]$ is an extended state representing the total disturbance with internal disturbance, external disturbance and the effect of evaluated error. By designing the following linear extended state observer (ESO) as

$$\begin{aligned} \dot{z}_o &= \boldsymbol{A}\boldsymbol{z}_o + \boldsymbol{B}\beta_c + \boldsymbol{L}\left(y - y_o\right) \\ y_o &= \boldsymbol{C}\boldsymbol{z}_o \end{aligned} \tag{22}$$

https://doi.org/10.1017/aer.2026.10162 Published online by Cambridge University Press

the state vector of the controlled system and the total disturbances can be simultaneously estimated. The observer gain $\boldsymbol{L}$ can be determined via

$$l_i = \frac{(n+1)!}{i!\,(n+1-i)!}\omega_o^i, i = 1, 2 \cdots n+1 \tag{23}$$

where ω_o is denoted as the bandwidth of the linear ESO, which should be manually adjusted to ensure the tracking performance. The detailed procedure can be found in Refs [39, 40].

3.2 Design of the feedback control law for states errors

Once the extended state observer is constructed, the estimated state vector $\boldsymbol{z}_{o1}$ and the estimated total disturbances $\boldsymbol{z}_{o2} = \bar{f}_o$ can be obtained. To eliminate the effects of the total disturbances, the feedback control law can be designed as follows

$$\beta_c(t) = \beta_0(t) - \frac{\boldsymbol{z}_{o2}(t)}{\bar{b}_0} \tag{24}$$

By substituting Equation (24) into the controlled ASE system defined in Equation (17), the closed-loop system can be simplified as

$$y_s^{(n)}(t) = \bar{b}_0\beta_0(t) + \left(\bar{f} - \bar{f}_o\right) \tag{25}$$

If the state errors $\boldsymbol{e}$ approach zero, the above closed-loop system can be simplified further into a linear system as

$$y_s^{(n)}(t) = \bar{b}_0\beta_0(t) \tag{26}$$

and the control input $\beta_0(t)$ can be given to control the linear system as

$$\beta_0(t) = -\frac{\boldsymbol{K}_r}{\bar{b}_0}\boldsymbol{z}_{o1}(t) \tag{27}$$

The controller gain $\boldsymbol{K}_r$ is given by

$$k_i = \frac{n!}{(i-1)!\,(n+1-i)!}\omega_c^{n+1-i}, \quad i = 1, 2 \cdots n \tag{28}$$

where ω_c is the bandwidth of the feedback controller, which should also be adjusted to ensure the stability of the closed-loop system.

The ultimate controller for transonic structural instabilities could be written as follows

$$\beta_c(t) = -\frac{\boldsymbol{K}_r}{\bar{b}_0}\boldsymbol{z}_{o1}(t) - \frac{\boldsymbol{z}_{o2}(t)}{\bar{b}_0} \tag{29}$$

The estimated state vector $\boldsymbol{z}_{o1}(t)$ and estimated total disturbances $\boldsymbol{z}_{o2}(t)$ can be obtained from Equation (22). It is noted that three parameters need to be regulated for synthesising the proposed control scheme, i.e. preliminary choice of $\bar{b}_0$, the bandwidth ω_o of the linear ESO and the bandwidth ω_c of the controller for state errors. By using the zero-order hold method, the linear ESO can be discretised as follows

$$\boldsymbol{z}_o(k+1) = (\boldsymbol{I} + \boldsymbol{A}T_s)\,\boldsymbol{z}_o(k) + T_s\left[\boldsymbol{B}\beta_c(k) + \boldsymbol{L}\left(y_s(k) - \hat{y}_s(k)\right)\right] \tag{30}$$

where T_s and k are the sampling time and time step, respectively. The discretised mathematical model of the proposed controller is given as

$$\beta_c(k) = -\frac{\boldsymbol{K}_r}{b_0}\boldsymbol{z}_{o1}(k) - \frac{\boldsymbol{z}_{o2}(k)}{b_0} \tag{31}$$

4.0 Case studies and discussions

In the following numerical simulations, the density-based compressible unsteady Reynolds-Averaged-Navier-Stokes flow solver is used to obtain the unsteady aerodynamic forces required for the

https://doi.org/10.1017/aer.2026.10162 Published online by Cambridge University Press

Table 1. *Structural parameters of the NACA 0012 aerofoil*

$\bar{x}_\alpha$	$\bar{r}_\alpha^2$	$\bar{a}$	ω_h	ω_α	μ	$\bar{S}_{h\beta}$	$\bar{S}_{\alpha\beta}$
0.0035	1.036	0	21.1 rad/s	32.66 rad/s	3,366	7.10×10^{-4}	5.80×10^{-4}

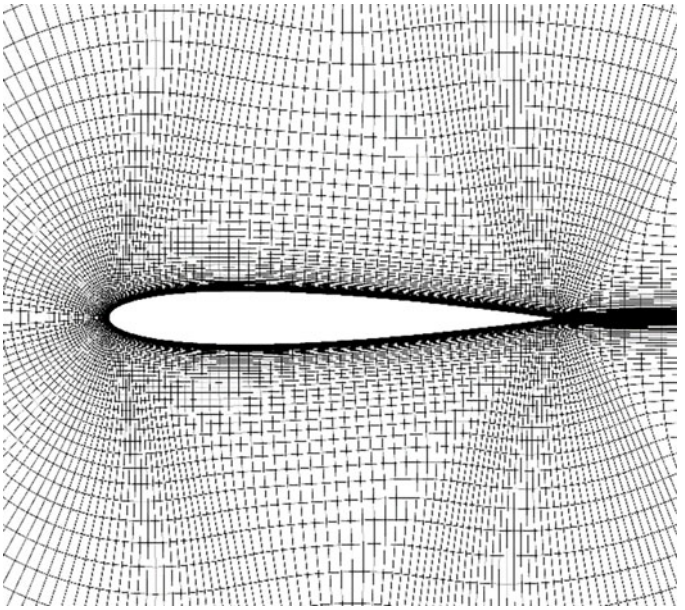


Figure 3. *Flow field grid of the NACA0012 aerofoil.*

identification process and direct aeroelastic simulations. The cell-centred finite volume scheme is used as the mesh discretisation method. For the convective terms, Roe's Flux-Difference Splitting (FDS) scheme combined with Monotone Upstream-Centered Schemes for Conservation Laws (MUSCL) interpolation is utilised to achieve high-order accuracy, while flux limiters ensure shock-capturing stability. The viscous terms are discretised using a central differencing scheme. For unsteady flow simulations, an implicit dual-time-stepping method is adopted for time advancement. A second-order implicit scheme is applied at the physical time level, and pseudo-time sub-iterations (τ-TS) are implemented to eliminate factorisation errors in pseudo-time, thereby restoring high-order temporal accuracy. The physical time step was set at 0.0001s in order to capture the buffet phenomenon. The exponential decay combined with trans-finite interpolation of interior mesh points is equipped for moving grids in aeroelastic simulations, and the Spalart-Allmaras model is chosen as the turbulent model in the study. The CFD simulations made in an AMAX CPU/graphics processing unit computer cluster and the validation of the flow solver can be found in the previous studies of the authors [39, 41], where unsteady aerodynamic forces and the flutter boundary were compared with the experiment results.

The aeroelastic and ASE phenomena of the NACA0012 aerofoil at Mach number 0.71 are studied via CFD, and the results are compared to verify the accuracy of the proposed nonlinear ROM. The extra-fine 1025×513 C-grid used in CFD computation is depicted in Fig. 3, which was downloaded from CFL3d. The structural parameters are listed in Table 1. The Reynolds number is 1.32×10^6 and the physical frequency ω is transformed into the reduced frequency $k = \omega b / V_\infty$ in the frequency comparisons. The large shock wave oscillations can be captured in the unsteady flow field calculation of a NACA0012 aerofoil at Mach 0.71 with a steady mean angle-of-attack, which is presented in Fig. 4, so that the complex aeroelastic phenomena, such as nodal-shaped oscillations, can be reproduced.

https://doi.org/10.1017/aer.2026.10162 Published online by Cambridge University Press

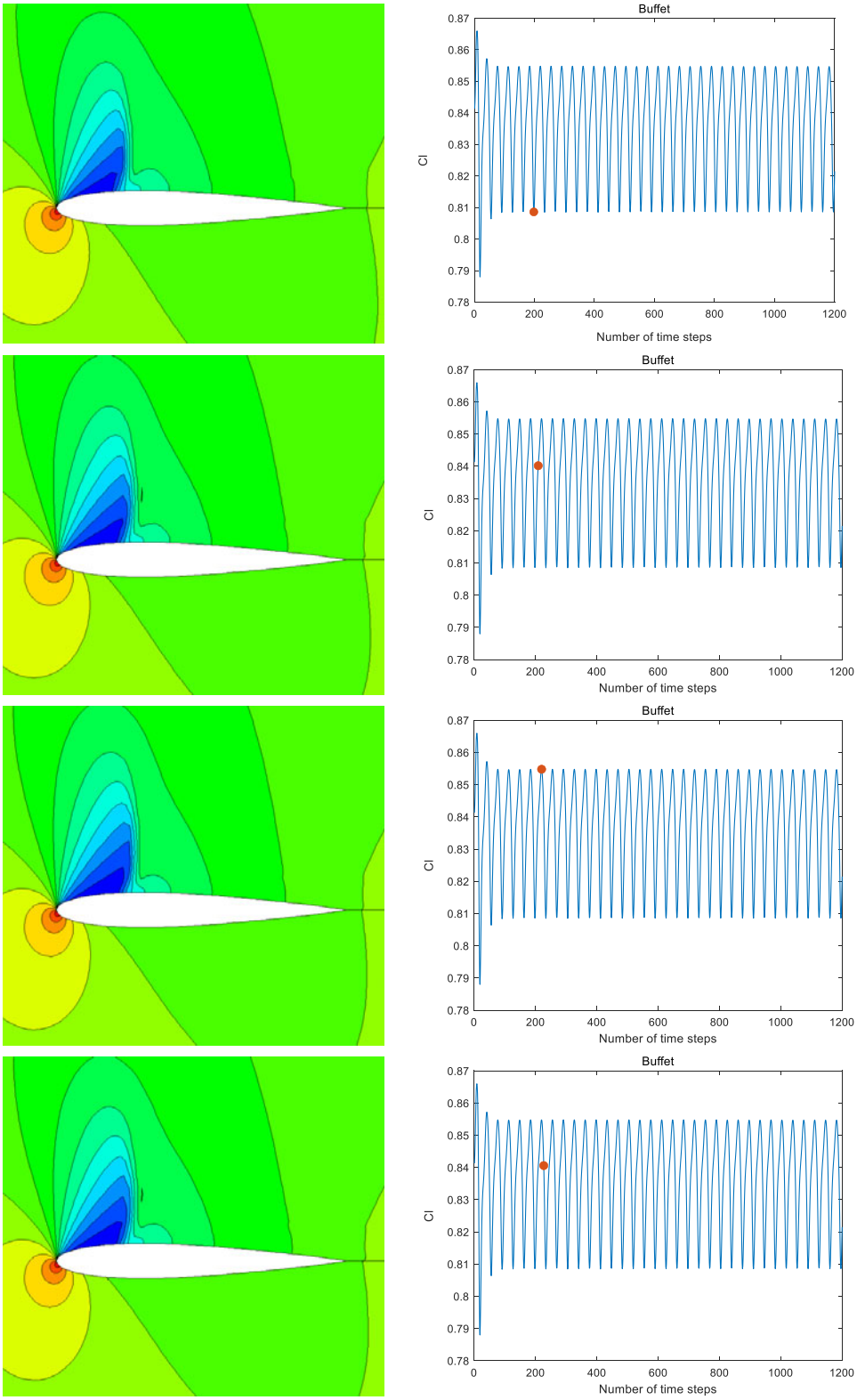


Figure 4. *Simulation of buffet phenomenon in unsteady flow fields.*

https://doi.org/10.1017/aer.2026.10162 Published online by Cambridge University Press

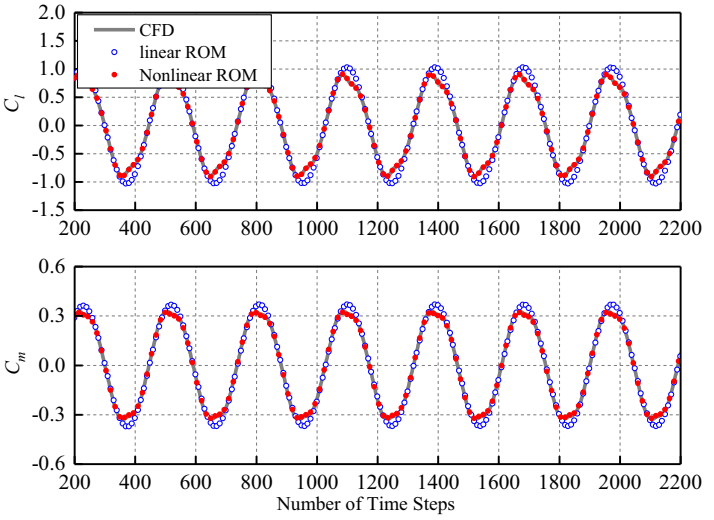


Figure 5. *Aerodynamic forces under the sinusoidal excitation of the NACA0012 aerofoil.*

4.1 Validation of reduced-order aerodynamic model

The first stage of the case studies is to establish the reduced-order model for aerodynamic forces using the impulsive signal and the FWGN signal. The amplitude of the impulsive signal is taken as a small value, say, 0.01. The parameters of the sinusoidal signal for the optimisation procedure are selected according to the LCOs at $V_\infty^* = 0.578$. The amplitude of the sinusoidal signal for the pitch is chosen as 0.088, and the physical frequency is set as 23.6 rad/s. The maximal amplitudes of the FWGN signal are determined as 1.63, 0.148 and 6.36 for the plunge, the pitch and the control surface motion, respectively. The frequency range of the first two degrees of freedom is the same, that is, from 0 to 62.8 rad/s, and for the control surface motion, the range is chosen from 0 to 157.0 rad/s.

The order of the linear part is finally determined to be 15 via the optimisation procedure. Figure 5 shows the comparison under the sinusoidal excitation used to determine the order of the linear part, and it can also be seen that the nonlinear ROM has higher accuracy in modeling aerodynamic forces with large amplitudes of structural vibrations. It should be noted that the nonlinear ROM compared in Fig. 5 is established after the identification of the nonlinear part. Figure 6 shows the comparison of the aerodynamic forces via different models for the FWGN excitation. The comparison presents that the nonlinear ROM can predict the aerodynamic forces more accurately for arbitrary structure vibrations than the linear ROM.

4.2 Structural and aerodynamic behaviours of a wing section in transonic buffeting flows

In this subsection, the ASE system is established via the procedure in Section 2, and the aeroelastic phenomena are investigated for the control surface fixed. The LCOs are firstly studied and the comparison of the LCO amplitudes at $V_\infty^* = 0.56$ is presented in Fig. 7. Now, the LCO amplitude of the plunge obtained via the ROM-based model is in good agreement with that of the CFD-based model, but the LCO amplitude of the pitch is slightly smaller than that of the CFD-based model.

The second nonlinear phenomenon of concern in the case study is the nodal-shaped oscillations, which may happen if the reduced velocity is much higher than the critical velocity of flutter. Figure 8 shows the time history of the structural vibration at $V_\infty^* = 0.621$, and Fig. 9 gives the amplitude of the Fourier spectrum of the time history. Nodal-shaped oscillations occur due to the variation in the phase-angle difference between the plunging and pitching displacements. The variation caused via the nonlinearity of the aerodynamic forces occurs because of the shock oscillations induced by interactions

https://doi.org/10.1017/aer.2026.10162 Published online by Cambridge University Press

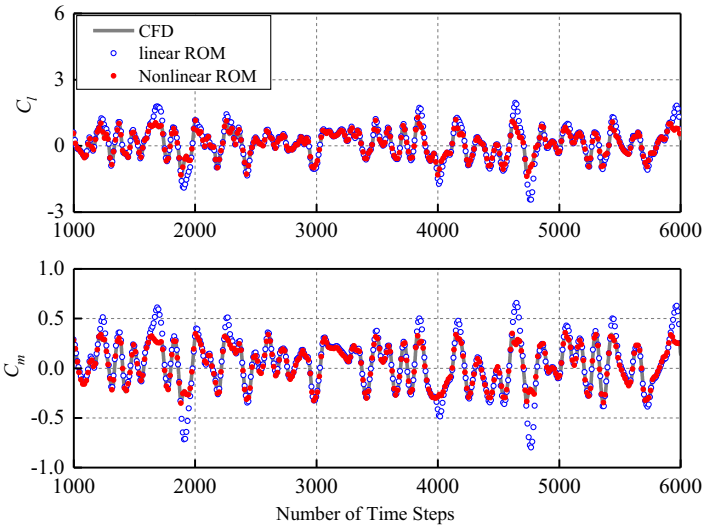


Figure 6. *Aerodynamic forces under FWGN excitation of the NACA0012 aerofoil.*

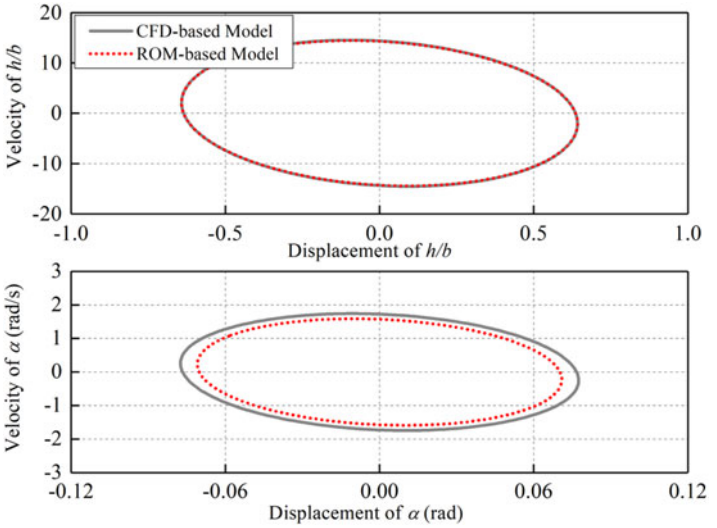


Figure 7. *Phase portraits of LCO of the NACA0012 aerofoil at* $V_\infty^* = 0.56$.

between shock-waves and intermittently separated shear layers. A detailed explanation about nodal-shaped oscillations can be found in Ref. [42]. Figures 8 and 9 show that the structural vibration obtained via the modified ROM-based model is in good agreement with that obtained via the CFD-based model, both in the time domain and the frequency domain. The envelope curves in Fig. 8 come from the interpolation of locally maximal values via the cubic splines. The maximal values and minimal values of the envelope curves are defined as the peaks and the valleys used for comparisons on structural vibrations at different reduced velocities.

Figures 10 and 11 give the aerodynamic forces obtained via CFD and ROM in the time domain and the frequency domain, respectively. The results show that the aerodynamic forces of the nodal-shaped oscillations exhibit high-frequency components as reported in previous studies, and the coupling between the structural vibration and the aerodynamic buffet may result in more high-frequency components. The comparisons of the aerodynamic forces show that the modified ROM captures the major frequency

https://doi.org/10.1017/aer.2026.10162 Published online by Cambridge University Press

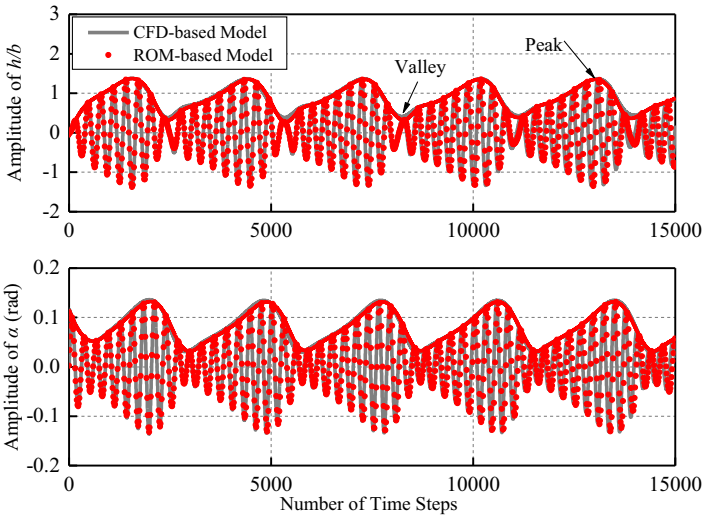


Figure 8. *Dynamic response of the aeroelastic model at* $V_{\infty}^{*} = 0.621$.

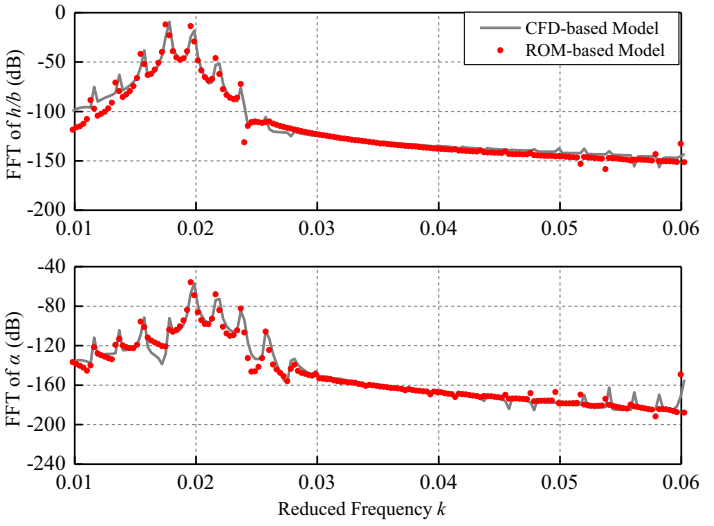


Figure 9. *The amplitude of the Fourier spectrum of nodal-shaped oscillations.*

components of the aerodynamic forces and reflects the main characteristics of aerodynamic forces in a high-frequency range.

Figure 12 gives the comparison of the buffeting oscillations between the ROM-based simulation and the CFD-based simulation at different reduced velocities. Moreover, Fig. 13 gives the dominant frequencies of the dynamic responses at the same range of reduced velocities. In Fig. 13, the 1st frequency and the 2nd frequency correspond to the highest peak and the second-highest peak, respectively. The 1st and 2nd frequencies of the plunge exchange positions, showing that the major frequency components of aerodynamic forces are different at different frequencies. The comparison shows that the nonlinear ROM has an excellent ability to predict the nodal-shaped oscillations at different reduced velocities. Then, Table 2 gives the comparison of the total CPU times for the CFD simulation and the nonlinear ROM simulation for the aeroelastic phenomena at different reduced velocities. The results well indicate

https://doi.org/10.1017/aer.2026.10162 Published online by Cambridge University Press

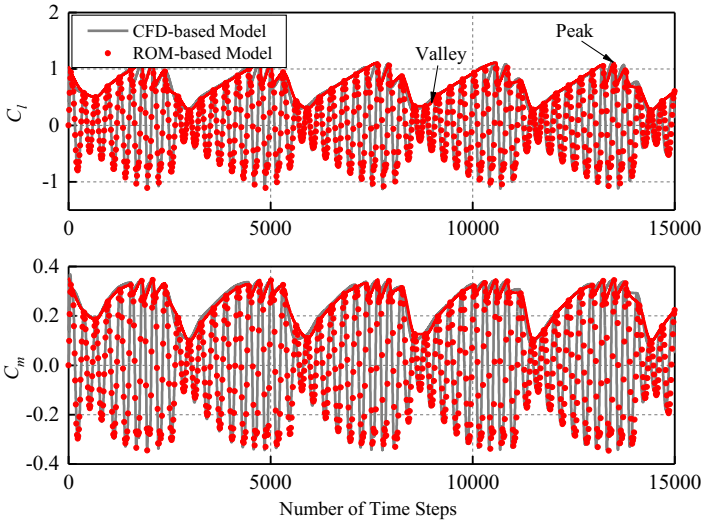


Figure 10. *Time history of aerodynamic forces at* $V_\infty^* = 0.621$.

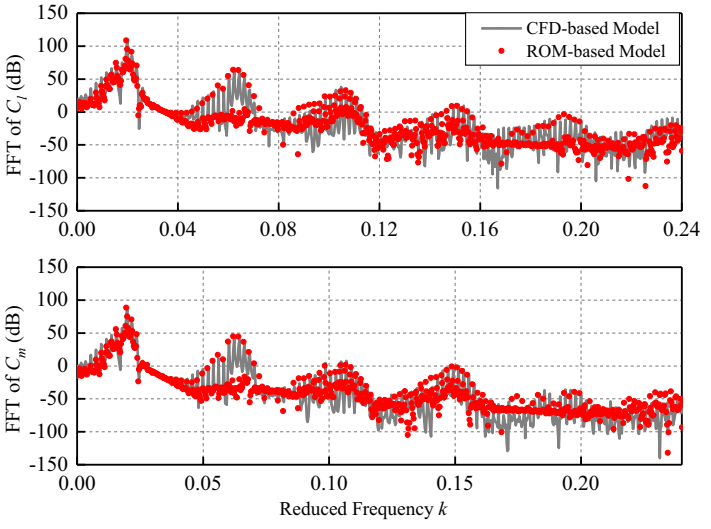


Figure 11. *The amplitude of the Fourier spectrum of aerodynamic forces in nodal-shaped oscillations.*

that the nonlinear ROM has an efficient ability to model the aeroelastic phenomena with high accuracy, even when the time of generating the training signals is taken into account.

4.3. Predictions of open-loop buffeting behaviours

This subsection compares the ASE behaviours induced via the control surface motions at two reduced velocities, with input signals of different amplitudes and frequencies. At the low reduced velocities, the amplitudes of the structural vibrations are small and the ASE system presents linear characteristics. When the reduced velocities go up, the ASE system presents nonlinear characteristics for large amplitudes of the structural vibrations.

The ASE behaviours at $V_\infty^* = 0.320$ with sinusoidal input are presented in Fig. 14. The amplitude and the frequency of the sinusoidal input are chosen as 1 deg and 3.6 Hz, which is close to the uncoupled

https://doi.org/10.1017/aer.2026.10162 Published online by Cambridge University Press

Table 2. *Comparison of the CPU times for CFD and nonlinear ROM simulations*

Method	Detail	Time
CFD	Nodal-shaped oscillations at 9 reduced velocities (20,000 time steps each)	157.5 h
Training signals	Pulse signal (200 time steps); Sinusoidal signal (1,000 time steps); FWGN signal (10,000 time steps)	9.9 h
ROM	ROM establishment and simulation at 125 reduced velocities (20,000 time steps each)	0.23 h+0.07 h

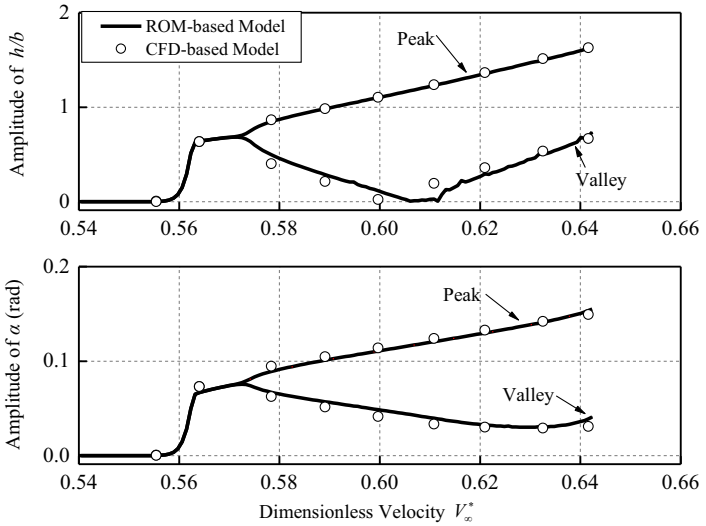


Figure 12. *Amplitudes of nodal-shaped oscillations vs. dimensionless velocity.*

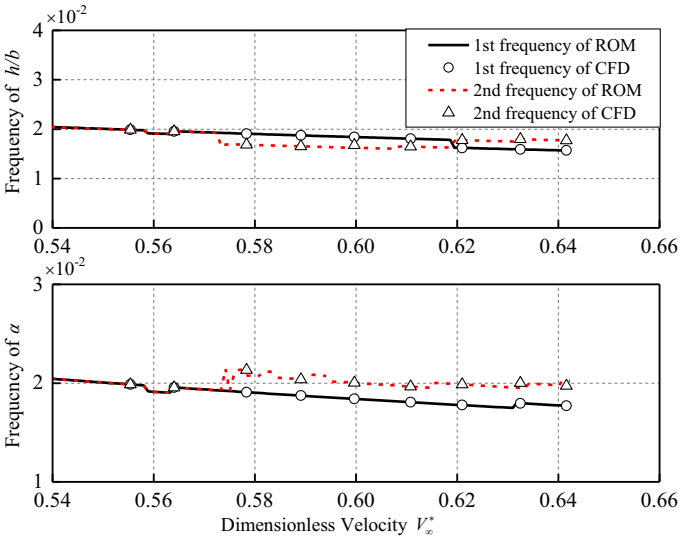


Figure 13. *Frequencies of nodal-shaped oscillations vs. dimensionless velocity.*

https://doi.org/10.1017/aer.2026.10162 Published online by Cambridge University Press

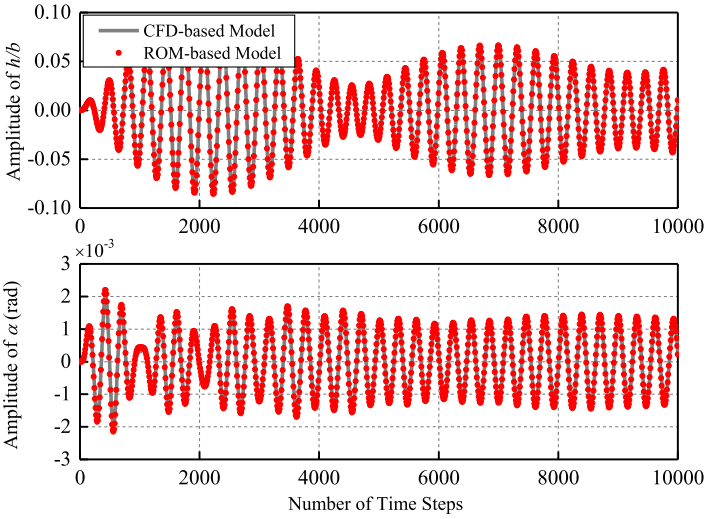


Figure 14. *Dynamic response of the aeroservoelastic model with the sinusoidal input at* $V_\infty^* = 0.320$.

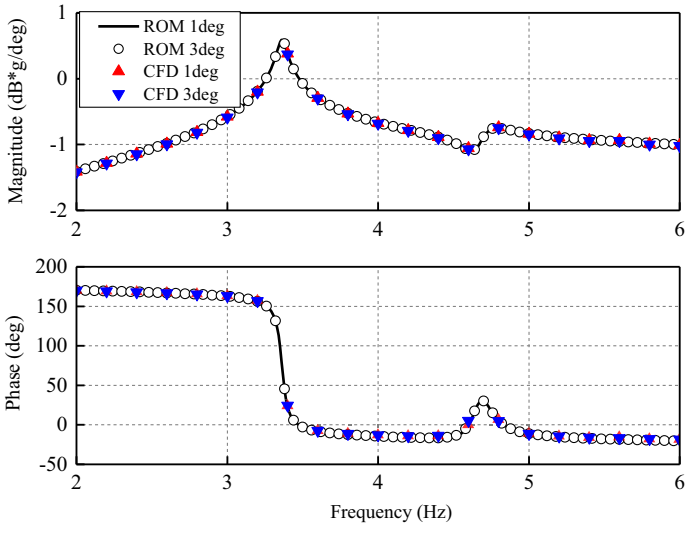


Figure 15. *Frequency-response function at* $V_\infty^* = 0.320$.

natural frequencies of the plunge. The transient response of the ASE systems can be accurately reproduced via the nonlinear ROM. As time goes on, the transient response disappears and the sinusoidal steady-state response appears because of the linear behaviour of the ASE system at low reduced velocity. Because of the fidelity importance of the frequency response of a linear system to be controlled, the comparison is made in Fig. 15 for the frequency responses via CFD-based and ROM-based ASE systems. The figure shows that the frequency responses are the same when the input signal amplitudes are 1 deg and 3 deg, respectively. This evidence verifies again that the ASE system at $V_\infty^* = 0.320$ presents linear characteristics. Hence, the CFD-based ASE systems can be replaced with the ROM-based in the design of the active control system at low reduced velocities.

The ASE behaviours at $V_\infty^* = 0.555$ under the sinusoidal input of different amplitudes and frequencies are also compared in the time domain. The responses under the sinusoidal input with 1deg and 3.6 Hz are shown in Fig. 16. The response is superimposed via two frequencies – one is the frequency of the

https://doi.org/10.1017/aer.2026.10162 Published online by Cambridge University Press

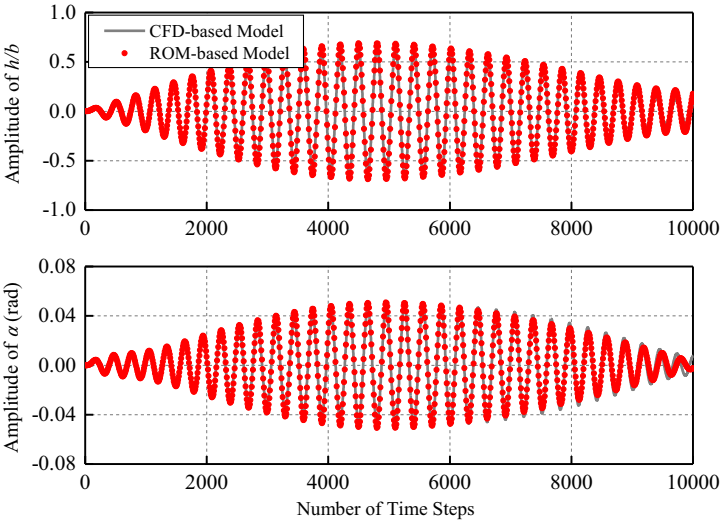


Figure 16. *Dynamic response stimulated via the sinusoidal input with 1 deg and 3.6 Hz at* $V_\infty^* = 0.555$.

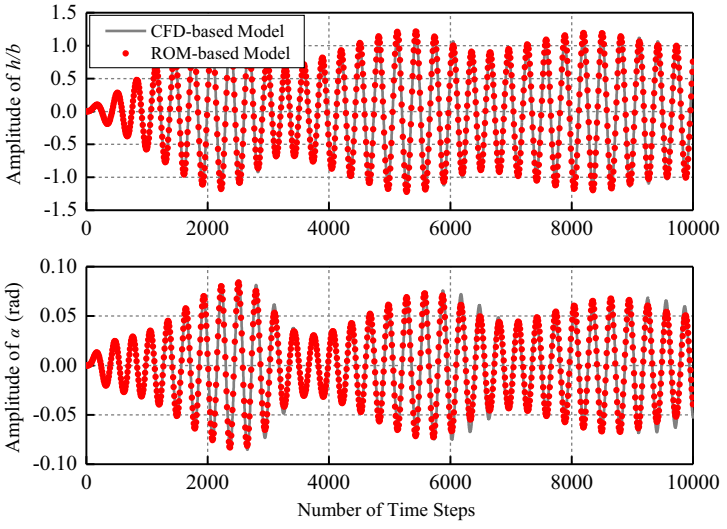


Figure 17. *Dynamic response stimulated via the sinusoidal input with 3 deg and 3.6 Hz at* $V_\infty^* = 0.555$.

control surface motions and the other is the frequency of the aerodynamic forces. The responses under the sinusoidal input with 3 deg and different frequencies are presented in Figs 17 and 18. On one hand, the aerodynamic forces are stimulated with nonlinear characteristics with larger amplitudes of input signals and structural vibrations. On the other hand, the rise and fall of the amplitudes of the structural vibrations in both figures are caused by the large nonlinear characteristics of the aerodynamic forces. The ROM-based ASE responses are compared with the CFD-based ones in Figs 17 and 18. The comparison shows that the ROM-based ASE models can accurately simulate the nonlinear characteristics of the aerodynamic forces for a long duration.

4.4 Performance for transonic buffeting control

This subsection gives the detailed parameters of the controller and verifies its control performance for the transonic buffeting vibrations of the ASE system. The order of the linear ACRC controller is set to 2.

https://doi.org/10.1017/aer.2026.10162 Published online by Cambridge University Press

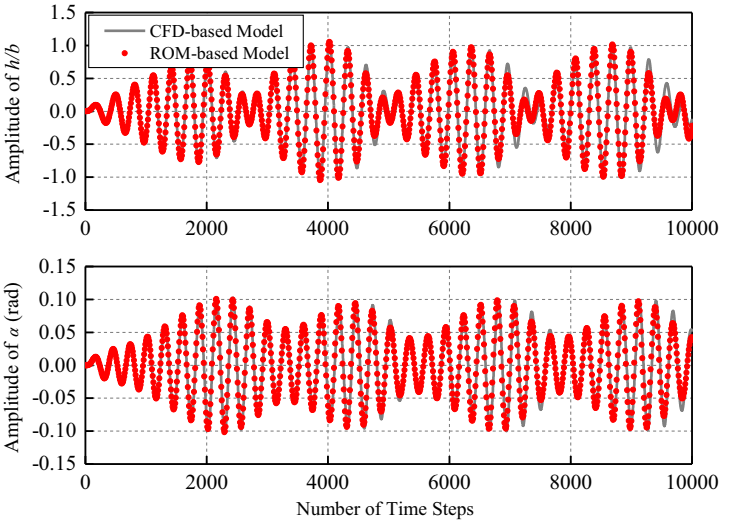


Figure 18. *Dynamic response stimulated via the sinusoidal input with 3 deg and 3.8 Hz at* $V_\infty^* = 0.555$.

Based on the adjustment principles, the parameters are eventually determined as $\bar{b}_0$=−40000, ω_o=250 and ω_c=18.

To check the control performance of the controller in the transonic region, the closed-loop ASE analysis is implemented at $V_\infty^* = 0.56$ and $V_\infty^* = 0.621$. The acceleration signal and the control command are given in Figs 19 and 20 to show the effectiveness of the controller at $V_\infty^* = 0.56$ and $V_\infty^* = 0.621$, respectively. The controller is first switched off and then switched on after a short moment. As shown in Fig. 19, the flutter instabilities can be observed before the controller is switched on. However, the flutter instabilities disappear when the controller is switched on at the moment of 25 s. A similar phenomenon can also occur for the open/closed ASE modeling at $V_\infty^* = 0.621$. The structural vibration for the first 5 s in Fig. 20 is actually the nodal-shaped oscillations in Fig. 8. When the controller is switched on at the moment of 5 s, the unstable structural vibrations, i.e. the nodal-shaped oscillations, gradually become stable as time goes on. The amplitudes of the control command are lower than 6deg in Fig. 19 and lower than 4.5 deg in Fig. 20. However, the on/off control simulations only verify the control performance of the controller. The controller is actually switched on during the whole process, and thus the control command will be much lower than that in the simulations. The controller increases the unstable boundary by 21.5%, from $V_\infty^* = 0.557$ to $V_\infty^* = 0.677$ based on the ROM-based ASE systems. Figure 21 shows the root-of-mean-squared (RMS) value of the acceleration response and the control surface at different reduced velocities under the same initial conditions. As shown in the figure, the RMS values of deflection of the control surface increase with an increase in the reduced velocities and the increasing rate becomes much larger when the reduced velocity is close to the unstable boundary of the closed-loop ASE system.

Now, the anti-interference abilities are checked for the present controller via numerical simulations, where the acceleration signal is mixed with the FWGN signal to simulate the effects of measured noises. The simulations are carried out at two typical reduced velocities $V_\infty^* = 0.56$ and $V_\infty^* = 0.621$. The amplitude of the noise is 10% of the maximal value of the accelerations in each simulation, and the frequency ranges of the noises are both from 20 to 50 Hz. The time histories of the acceleration signals and control commands in two typical reduced velocities are given in Figs 22 and 23, respectively. The changing process of the controller is the same as the process in the simulations without FWGN. In the two figures, the structural vibrations cannot be suppressed completely due to the noise interference, but they can be reduced to a small range. That is, the controller has good anti-interference abilities to suppress the structural instability with measured noises. The effects of measured noises at other reduced velocities are also verified. The RMS responses of the real acceleration and the control surface at different reduced

https://doi.org/10.1017/aer.2026.10162 Published online by Cambridge University Press

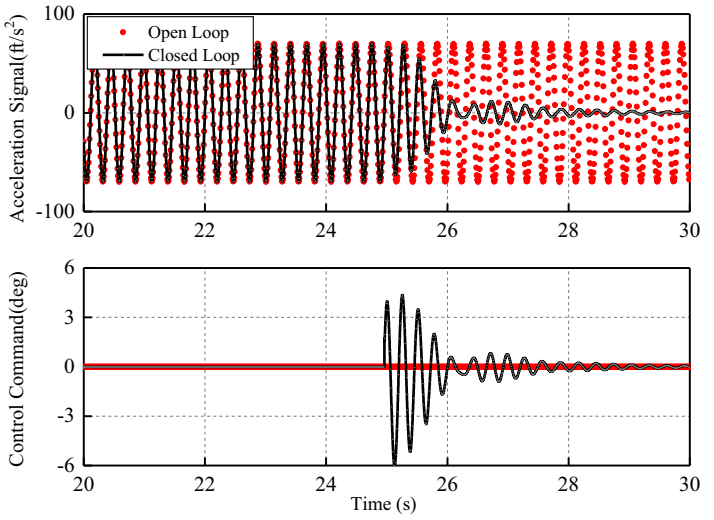


Figure 19. *Input and output signals of the controller for* $V_\infty^* = 0.56$.

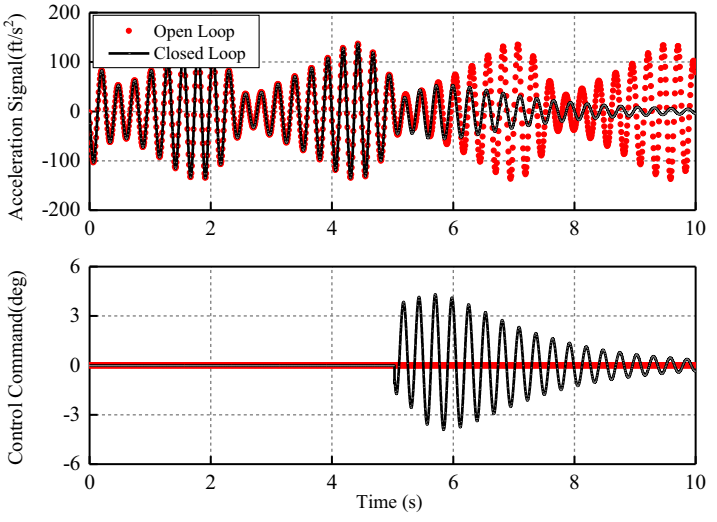


Figure 20. *Input and output signals of the controller for* $V_\infty^* = 0.621$.

velocities under zero initial conditions and the same measured noise are shown in Fig. 24. Although the RMS deflection of the real acceleration increases with an increase in the reduced velocity, the RMS deflection of the control surface nearly remains constant. The results make it clear that the energy consumed by the controller for suppressing the measured noise is the same for different velocities. However, the amplitude of structural vibration induced via the measured noise can be larger for higher reduced velocity.

Finally, the verification turns to the ability of the controller for a possible time delay in the control loop. The following simulations present the performance of the controller with a time delay for two reduced velocities. The results show that the tolerance interval of the time delay at $V_\infty^* = 0.56$ is 0∼50 ms, while the tolerance interval of the time delay at $V_\infty^* = 0.621$ decreases to 0∼5 ms. Figures 25 and 26 give the numerical simulations for $V_\infty^* = 0.56$ with a time delay of 50 ms and for $V_\infty^* = 0.621$ with a time delay of 5 ms, respectively. The acceleration signals in two simulations decrease slowly, and the

https://doi.org/10.1017/aer.2026.10162 Published online by Cambridge University Press

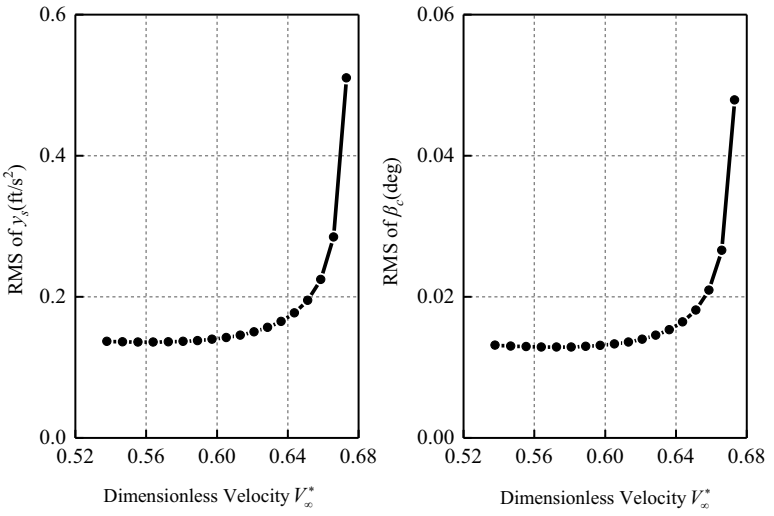


Figure 21. *RMS responses for the closed-loop system.*

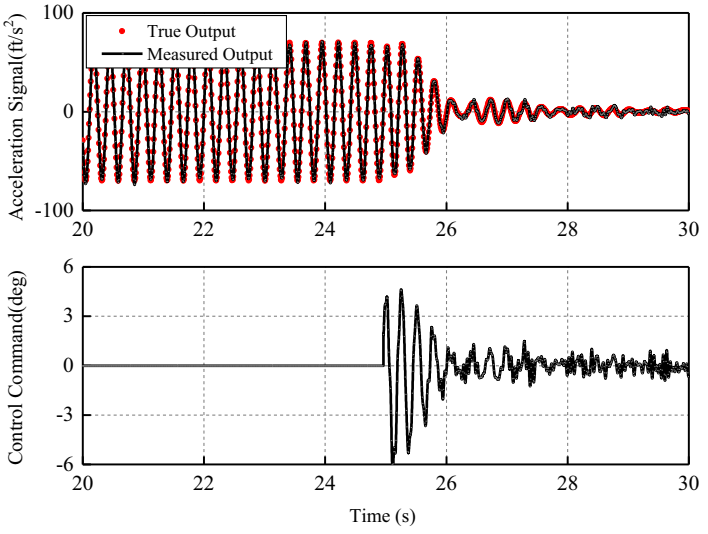


Figure 22. *Input and output signals of the controller with high-frequency noise for* $V_\infty^* = 0.56$.

controller fails for larger time delays. Unlike the controller's anti-interference capabilities, introducing a time delay in the control loop negatively affects the controller's ability to suppress structural instabilities when there are nonlinearities introduced by buffet. However, the controller can accept a short time delay to suppress the transonic buffeting vibrations.

5.0 Conclusions

The study presents the transonic buffeting control based on a novel nonlinear aeroservoelastic model of reduced-order, and the numerical validations of a two-dimensional aeroservoelastic system in a buffeting in order to analyse the aeroelastic and aeroservoelastic vibrations computed via computational fluid dynamics and reduced-order modeling. The comparisons verify the prediction accuracy of the presented

https://doi.org/10.1017/aer.2026.10162 Published online by Cambridge University Press

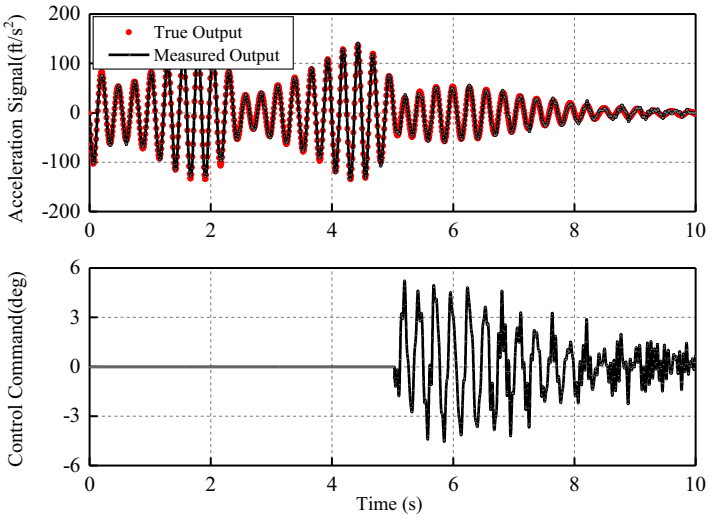


Figure 23. *Input and output signals of the controller with high-frequency noise for* $V_\infty^* = 0.621$.

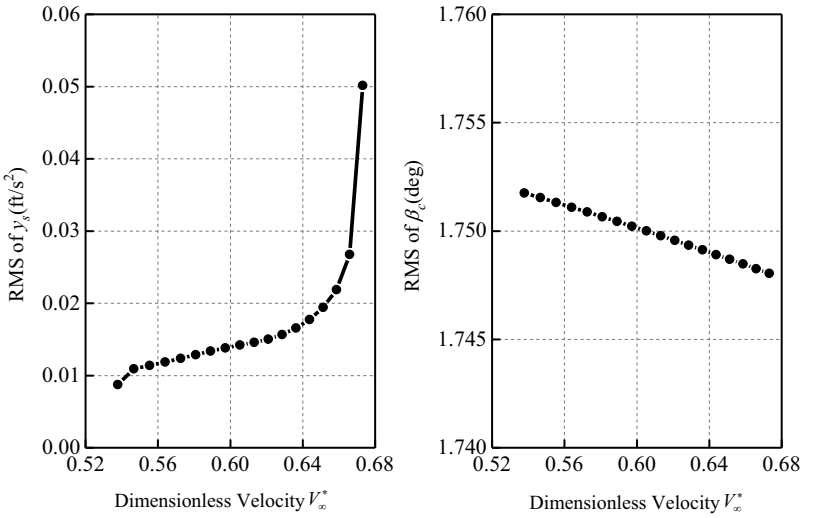


Figure 24. *RMS responses for the closed-loop system with measured noise.*

aeroservoelastic model of reduced-order for both linear and nonlinear phenomena of buffeting. Based on the nonlinear reduced-order modeling, the control performance of the transonic buffeting controller is verified. The results show that the proposed control law can effectively control the structural vibrations with buffeting and can deal with measured noises and time delays.

The study shows that the structural vibrations of an aerofoil system with aerodynamic instabilities can be more complex than flutter or LCOs. The numerical simulations indicate that the buffeting has a strong impact on the ability of the controller for time delay resistance. However, the anti-interference abilities of the controller are the same regardless of the buffeting and reduced velocities. In the design of a transonic buffeting control, the time delay resistance of the controller needs to receive more attention than the anti-interference abilities.

The study touches upon the nonlinear reduced-order modeling for a two-dimensional aerofoil system with a control surface only, but the generalisation to a practical wing model including more elastic modes is straightforward. It is possible to use the single composite-input/eigensystem realization algorithm

https://doi.org/10.1017/aer.2026.10162 Published online by Cambridge University Press

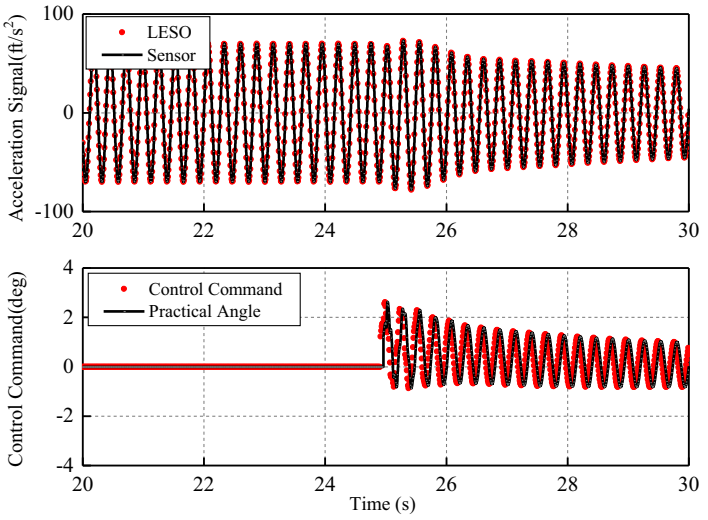


Figure 25. *Input and output signals of the controller with a time delay for* $V_\infty^* = 0.56$.

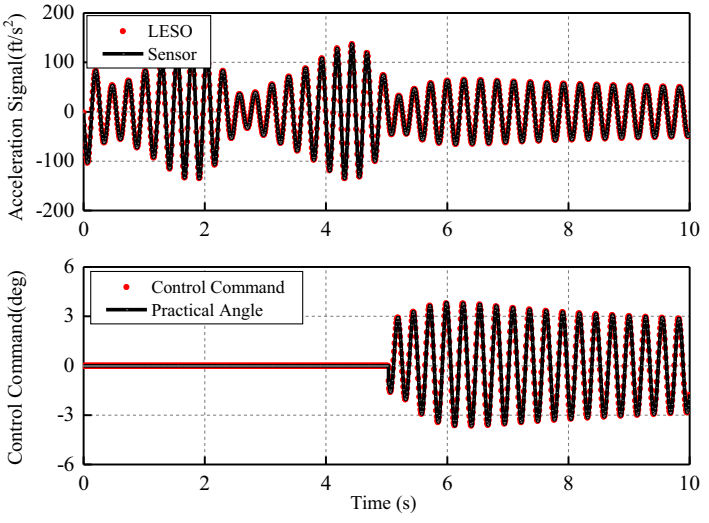


Figure 26. *Input and output signals of the controller with a time delay for* $V_\infty^* = 0.621$.

(SCI/ERA) to identify the linear part and to apply the identification of the nonlinear part to training nonlinear ROMs for the aircraft models. The following work may focus on making use of the nonlinear ROMs and active control systems for the aircraft models with aerodynamic instabilities.

Acknowledgements. This work was supported by the National Natural Science Foundation of China (Grant No. 12402007).

References

[1] Borglund, D. and Kuttenkeuler, J. Active wing flutter suppression using a trailing edge flap, *J. Fluids Struct.*, 2002, **16**, (3), pp 271–294.
[2] Waszak, M.R. Modeling the benchmark active control technology wind-tunnel model for application to flutter suppression, *21st Atmospheric Flight Mechanics Conference*, AIAA Paper 1996-3437, July 1996.
[3] Bernelli-Zazzera, F., Mantegazza, P. and Mazzoni, G. Active flutter suppression using recurrent neural networks, *J. Guid. Control Dyn.*, 2000, **23**, (6), pp 1030–1036.

https://doi.org/10.1017/aer.2026.10162 Published online by Cambridge University Press

[4] Haley, P. and Soloway, D. Generalized predictive control for active flutter suppression, *J. Guid. Control Dyn.*, 2001, **24**, (1), pp 154–159.
[5] Mukhopadhyay, V., Newsom, J.R. and Abel, I. Reduced-order optimal feedback control law synthesis for flutter suppression, *J. Guid. Control Dyn.*, 1982, **5**, (4), pp 389–395.
[6] Mordechay, K. Design for active flutter suppression and gust alleviation using state-space aeroelastic modeling, *J. Aircr.*, 1982, **19**, (3), pp 221–227.
[7] Mukhopadhyay, V. Flutter suppression control law design and testing for the active flexible wing, *J. Aircr.*, 1995, **32**, (1), pp 45–51.
[8] Andrighettoni, M. and Mantegazza, P. Multi-input/multi-outputadaptive active flutter suppression for a wing model, *J. Aircr.*, 1998, **35**, (3), pp 462–469.
[9] Huang, R., Zhao, Y.H. and Hu, H.Y. Wind-tunnel tests for active flutter control and closed-loop flutter identification, *AIAA J.*, 2016, **54**, (7), pp 2089–2099.
[10] Giannelis, N.F., Vio, G.A. and Levinski, O. A review of recent developments in the understanding of transonic shock buffet, *Prog. Aerosp. Sci.*, 2017, **92**, pp 39–84.
[11] Poplingher, L., Raveh, D.E. and Dowell, E.H. Modal analysis of transonic shock buffet on 2D airfoil, *AIAA J.*, 2019, **57**, (7), pp 2851–2866.
[12] Lee, B.H.K. Vertical tail buffeting of fighter aircraft, *Prog. Aerosp. Sci.*, 2000, **36**, (3), pp 193–279.
[13] Raveh, D.E., Numerical study of an oscillating airfoil in transonic buffeting flows, *AIAA J.*, 2009, **47**, (3), pp 505–515.
[14] Caruana, D., Corrège, M., Reberga, O., Despré, C. and Mignosi, A. Buffet and buffeting active control, *Fluids 2000 Conference and Exhibit*, pp 2000–2609.
[15] Molton, P., Dandois, J., Lepage, A., Brunet, V. and Bur, R. Control of buffet phenomenon on a transonic swept wing, *AIAA J.*, 2013, **51**, (4), pp 761–772.
[16] Caruana, D., Mignosi, A., Corrège, M., Le Pourhiet, A. and Rodde, A.M. Buffet and buffeting control in transonic flow, *Aerosp. Sci. Technol.*, 2005, **9**, (7), pp 605–616.
[17] Gao, C., Zhang, W. and Ye, Z. Numerical study on closed-loop control of transonic buffet suppression by trailing edge flap, *Comput. Fluids*, 2016, **132**, pp 32–45.
[18] Da Ronch, A., McCracken, A.J., Badcock, K.J., Widhalm, M. and Campobasso, M.S. Linear frequency domain and harmonic balance predictions of dynamic derivatives, *J. Aircr.*, 2013, **50**, (3), pp 694–707.
[19] Da Ronch, A., Badcock, K., Wang, Y., Wynn, A. and Palacios, R. Nonlinear model reduction for flexible aircraft control design, *AIAA Atmospheric Flight Mechanics Conference*, 2012, 4404.
[20] Zimmermann R and Görtz S. Improved extrapolation of steady turbulent aerodynamics using a non-linear POD-based reduced order model, *Aeronaut. J.*, 2012, **116**, (1184), pp 1079–1100.
[21] Zhang, W. and Ye, Z., Control law design for transonic aeroservoelasticity, *Aerosp. Sci. Technol.*, 2007, **11**, (2), pp 136–145.
[22] Danowsky, B.P., Thompson, P.M., Farhat, C., Lieu, T., Harris, C. and Lechniak, J., Incorporation of feedback control into a high-fidelity aeroservoelastic fighter aircraft model, *J. Aircr.*, 2010, **47**, (4), pp 1274–1282.
[23] Lindhorst, K., Haupt, M.C. and Horst, P. Reduced-order modelling of non-linear, transient aerodynamics of the HIRENASD wing, *Aeronaut. J.*, 2016, **120**, (1226), pp 601–626.
[24] Gao, W., Jiang, W., Li, Q. and Lu, B. Linear parameter-varying model order reduction and control design of FLEXOP demonstrator aircraft, *Aeronaut. J.*, 2025, **129**, (1339), pp 1–22.
[25] Moreno, C.P., Seiler, P.J. and Balas, G.J., Model reduction for aeroservoelastic systems, *J. Aircr.*, 2014, **51**, (1), pp 280–290.
[26] Liu, H., Hu, H., Zhao, Y. and Huang, R. Efficient reduced-order modeling of unsteady aerodynamics robust to flight parameter variations, *J. Fluids Struct.*, 2014, **49**, (1), pp 728–741.
[27] Yang, Z., Huang, R., Liu, H., Zhao, Y. and Hu, H. An improved nonlinear reduced-order modeling for transonic aeroelastic systems, *J. Fluids Struct.*, 2020, **94**, (1), p 102926.
[28] Ghoreyshi, M., Cummings, R.M., Ronch, A.D. and Badcock, K.J. Transonic aerodynamic load modeling of X-31 aircraft pitching motions, *AIAA J.*, 2013, **51**, (10), pp 2447–2464.
[29] Huang, R., Li, H., Hu, H. and Zhao, Y. Open/closed-loop aeroservoelastic predictions via nonlinear, reduced-order aerodynamic models, *AIAA J.*, 2015, **53**, (7), pp 1812–1824.
[30] Huang, R., Liu, H., Yang, Z., Zhao, Y. and Hu, H. Nonlinear reduced-order models for transonic aeroelastic and aeroservoelastic problems, *AIAA J.*, 2018, **56**, (9), pp 3718–3731.
[31] Moré, J.J. The Levenberg-Marquardt Algorithm: Implementation and Theory, Numerical Analysis, Springer, 1978, Berlin, Heidelberg, pp 105–116.
[32] Yang, Z., Huang, R., Liu, H., Zhao, Y. and Hu, H. An improved nonlinear reduced-order modeling for transonic aeroelastic systems, *J. Fluids Struct.*, 2020, **94**, p 102926.
[33] Mannarino, A and Dowell, E.H. Reduced-order models for computational-fluid-dynamics-based nonlinear aeroelastic problems, *AIAA J.*, 2015, **53**, (9), pp 2671–2685.
[34] Theodorsen, T. General theory of aerodynamic instability and the mechanism of flutter, No. NACA-TR-496, 1979.
[35] Waszak, M. Modeling the benchmark active control technology wind-tunnel model for application to flutter suppression, *21st Atmospheric Flight Mechanics Conference*, 1996, 3437.
[36] Edwards, J.W., Bennett, R.M., Whitlow, W. Jr and Seidel, D.A. Time-marching transonic flutter solutions including angle-of-attack effects, *J. Aircr.*, 1983, **20**, (11), pp 899–906.
[37] Han J.Q. Auto disturbance rejection controller and it's applications, *Control Decis.*, 1998, **13**, (1), pp 19–23.
[38] Gao, Z., Huang, Y. and Han, J. An alternative paradigm for control system design, *Proceedings of the 40th IEEE Conference on Decision and Control*, IEEE, 2001, 5, pp 4578–4585.

https://doi.org/10.1017/aer.2026.10162 Published online by Cambridge University Press

[39] Yang, Z., Huang, R., Zhao, Y. and Hu, H. Design of an active disturbance rejection control for transonic flutter suppression, *J. Guid. Control Dyn.*, 2017, **40**, (11), pp 2905–2916.
[40] Yang, Z., Huang, R., Zhao, Y. and Hu, H. Transonic flutter suppression for a three-dimensional elastic wing via active disturbance rejection control, *J. Sound Vib.*, 2019, **445**, pp 168–187.
[41] Huang, R., Hu, H. and Zhao, Y., Nonlinear reduced-order modeling for multiple-input/multiple-output aerodynamic systems, *AIAA J.*, 2014, **52**, (6), pp 1219–1231.
[42] Zhang, W., Gao, C., Liu, Y., Ye, Z. and Jiang, Y. The interaction between flutter and buffet in transonic flow, *Nonlinear Dyn.*, 2015, **82**, (4), pp 1851–1865.

Cite this article: Yang Z., Zhang Z., Zhang M. and He S. (2026). Transonic buffeting control via a nonlinear aeroservoelastic model of reduced-order. *The Aeronautical Journal*, **130**, 2319–2342. https://doi.org/10.1017/aer.2026.10162

https://doi.org/10.1017/aer.2026.10162 Published online by Cambridge University Press